ACSNANO
www.acsnano.org
ARTICLE

Analysis of Time-Varying, Stochastic Gas Transport through Graphene Membranes

Lee W. Drahushuk,[†] Luda Wang,[‡,§] Steven P. Koenig,[∥,⊥] J. Scott Bunch,[#,▽] and Michael S. Strano*[,†]

[†]Department of Chemical Engineering, and [‡]Department of Mechanical Engineering, Massachusetts Institute of Technology, Cambridge, Massachusetts 02139, United States

[§]Department of Mechanical Engineering, University of Colorado at Boulder, Boulder, Colorado 80309, United States

[∥]Department of Physics, National University of Singapore, 117542 Singapore

[⊥]Graphene Research Centre, National University of Singapore, 117546 Singapore

[#]Department of Mechanical Engineering, Boston University, Boston, Massachusetts 02215, United States

[▽]Division of Materials Science and Engineering, Boston University, Brookline, Massachusetts 02446, United States

Supporting Information

ABSTRACT: **Molecular transport measurements through isolated nanopores can greatly inform our understanding of how such systems can select for molecular size and shape. In this work, we present a detailed analysis of experimental gas permeation data through single layer graphene membranes under batch depletion conditions parametric in starting pressure for He, H_2, Ne, and CO_2 between 100 and 670 kPa. We show mathematically that the observed intersections of the membrane deflection curves parametric in starting pressure are indicative of a time dependent membrane permeance (pressure normalized molecular flow). Analyzing these time dependent permeance data for He, Ne, H_2, and CO_2 shows remarkably that the latter three gases exhibit discretized permeance values that are temporally repeated. Such quantized fluctuations (called "gating" for liquid phase nanopore and ion channel systems) are a hallmark of isolated nanopores, since small, but rapid changes in the transport pathway necessarily influence a single detectable flux. We analyze the fluctuations using a Hidden Markov model to fit to discrete states and estimate the activation barrier for switching at 1.0 eV. This barrier is and the relative fluxes are consistent with a chemical bond rearrangement of an 8−10 atom vacancy pore. Furthermore, we use the relations between the states given by the Markov network for few pores to determine that three pores, each exhibiting two state switching, are responsible for the observed fluctuations; and we compare simulated control data sets with and without the Markov network for comparison and to establish confidence in our evaluation of the limited experimental data set.**

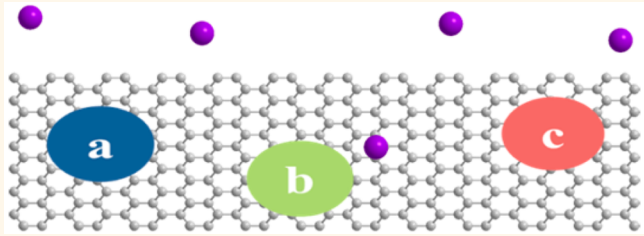

KEYWORDS: *graphene membrane, parametric, molecular transport, deflection curve, activation barrier, stochastic*

Applications of membrane separations that take advantage of graphene's one atomic layer thickness and regular lattice structure are an emerging area of research. Pristine single layer graphene is impermeable to even the smallest of gases,[1] though recent work has shown there is a mechanism for proton transport.[2] However, by opening well-defined pores in the graphene lattice, large separation factors can be achieved. The atomic thickness of the graphene layer is the optimal limit for absolute permeation rate, which is typically limited by the thickness of the membrane material. A variety of simulations and calculations have looked at separations of gas[3−17] and liquid[18−23] systems. However, experimental and theoretical analyses of gas phase transport through isolated graphene nanopores have been few in the literature. In this work, we develop a mathematical formalism that allows one to detect and analyze stochastic gas phase fluxes from graphene membranes, extracting activation energies of pore rearrangements, and even identifying contributions from multiple, isolated pores.

There have been a few experimental demonstrations of membrane systems from single or few layer graphene that have been realized. A study by the Bunch group showed that pores created by UV ozone etching in mechanically exfoliated graphene suspended over microcavities in silicon and demonstrating molecular sieving, creating high selectivities between gas species of differing molecular size.[24] Work using the intrinsic defects in CVD grown graphene transferred onto polycarbonate track etched membranes in aqueous systems was able to demonstrate modest separation of larger molecules and

Received: September 17, 2015
Accepted: December 21, 2015

DOI: 10.1021/acsnano.5b05870
ACS Nano XXXX, XXX, XXX−XXX

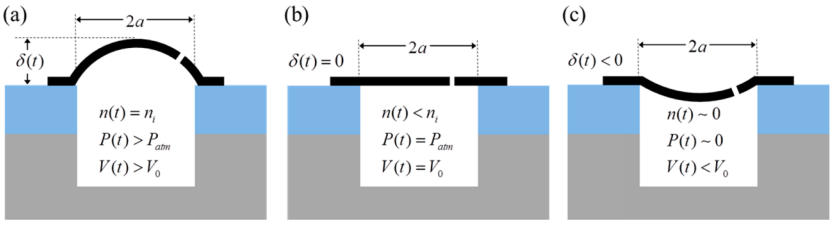

Figure 1. Depiction of experimental system depicting microcavity in Si/SiO_2 (gray/blue) covered by a single layer graphene membrane (black bar) with randomly located pore(s) represented by a break in the black bar. Illustrations are labeled with variables as used in models; *a* for microcavity radius, δ for membrane deflection, *n* for moles of gas in microcavity, *P* for internal microcavity pressure, and *V* for microcavity volume enclosed by graphene. Panes depict variation over the course of a typical experimental run (a) at the start, (b) in the middle at zero deflection, and (c) at the end.

investigated layer stacking to reduce the leakage through those intrinsic defects.[25,26] Other work with the aqueous phase used a contact seal between a micrometer scale pipet tip and graphene at the air−water interface to measure conductivity through CVD graphene.[27] Another study used focused ion beam to create pore size distributions centered on multiple sizes from 8 nm to 1 μm in two stacked layers of CVD grown graphene, transferred to and supported on a SiN_x membrane, and demonstrated Knudsen selectivity based on the square root of molecular weight typical of classical effusion.[28] Recent work demonstrated proton transport through pristine, mechanically exfoliated graphene, as well as other 2D crystals, coated with Nafion and suspended across a hole drilled through SiN_x.[2]

The Bunch group's demonstration of molecular sieving[24] and investigation of mechanical properties[29] used mechanically exfoliated graphene suspended over a microcavity in a silicon wafer to form a membrane between the gas trapped in the microcavity and the atmosphere; measuring the deflection of the graphene surface over time was used to track the transport of gas. While this technique is not scalable, it does offer the unique advantage of being able to measure the transport characteristics of a single or few subnanometer pores, giving a window toward the fundamental transport characteristics of graphene. Recent work with this platform demonstrates switchable gating of the transport by gold nanoclusters on the graphene membrane surface, as well as smaller but significant fluctuations in transport without gold nanoclusters present.[30]

In this work, we present the first detailed mathematical analysis of stochastic gas permeation through any membrane/nanopore system. We validate the model using experimental results from our previous work on single layer graphene membranes under batch depletion conditions parametric in starting pressure for He, H_2, Ne, and CO_2 between 100 and 670 kPa.[30] The model enables one to use membrane deflection curves parametric in starting pressure to confirm a time dependent membrane permeance (pressure normalized molecular flow). Stochastic fluctuations of the gas permeance can be analyzed using a Hidden Markov model to fit discrete states and estimate the activation barrier for switching. Our formalism also teaches how to use the relations between the states given by the Markov network for a collection of pores to determine the operative number that describes the data.

RESULTS AND DISCUSSION

Analysis of AFM Membrane Deflection Curves. Figure 1 illustrates the typical course of an experimental run, in which the deflection of a graphene membrane over a pressurized microcavity is monitored with atomic force microscopy (AFM). The measured deflection can be correlated to the state of the microcavity defined in terms of the moles of gas, pressure, and volume enclosed by the graphene. As shown in Figure 1c, the graphene is typically deflected downward at the end of an experiment with smaller gases because the air gases enter much more slowly than the charged gas evacuates the microcavity. Data from two different samples is presented here: sample 1 was formed with a suspended single layer of graphene and sample 2 was formed with a suspended bilayer of graphene.

From mechanical models of thin films, the pressure within the cavity can be related to the observed deflection (δ) according to the following relation[31]

$$P(\delta(t)) = \frac{EwK(\upsilon)}{a^4}\delta(t)^3 + \frac{4S_0}{a^2}\delta(t) + P_{\text{atm}} \quad (1)$$

where E = 1 TPa is the Young's modulus, w = 0.34 nm is the film thickness, $K(\nu)$ = 3.09 is a constant determined by Hencky's solution and the system geometry, S_0 = 0.1 N/m is the initial surface tension, and a is the well radius.[29] The thickness and Young's modulus of single layer graphene are not precisely defined; however, the reported values fit deflection data collected at known pressures. Similarly, the volume of the microcavity can be described by

$$V(\delta(t)) = C(\upsilon)a^2\pi\ \delta(t) + V_0 \quad (2)$$

where $C(\nu)$ = 3.09 is a constant determined by Hencky's solution and the system geometry, and V_0 is the volume of the microcavity with zero deflection of the graphene sheet. The gases considered in this work can be described by the ideal gas law, as shown in eq 3, but our results easily extend to more complex equations of state.

$$n(t) = \frac{P(\delta(t))\ V(\delta(t))}{RT} \quad (3)$$

Here, n is the moles of gas, P is the microcavity absolute pressure, V is the microcavity volume, T is the temperature, and R is the ideal gas constant. A mass balance on the permeating gas relates the rate of change of enclosed gas (dn/dt) to the sum of the gas flow(s) through the pore(s), $\dot{n}_{\text{pore}}$, and the leakage through the microcavity edges, $\dot{n}_{\text{background}}$. Previous work has shown that the molar flow through the pore is one to several orders of magnitude larger than the background leakage depending on the gas, based on comparing results before and after etching and pore formation;[30] therefore, we will treat $\dot{n}_{\text{background}}$ as negligible in subsequent analyses, as summarized in eq 4.

$$\frac{dn(t)}{dt} = \dot{n}_{\text{pore}}(t) + \dot{n}_{\text{background}}(t) \approx \dot{n}_{\text{pore}}(t) \quad (4)$$

DOI: 10.1021/acsnano.5b05870
ACS Nano XXXX, XXX, XXX−XXX

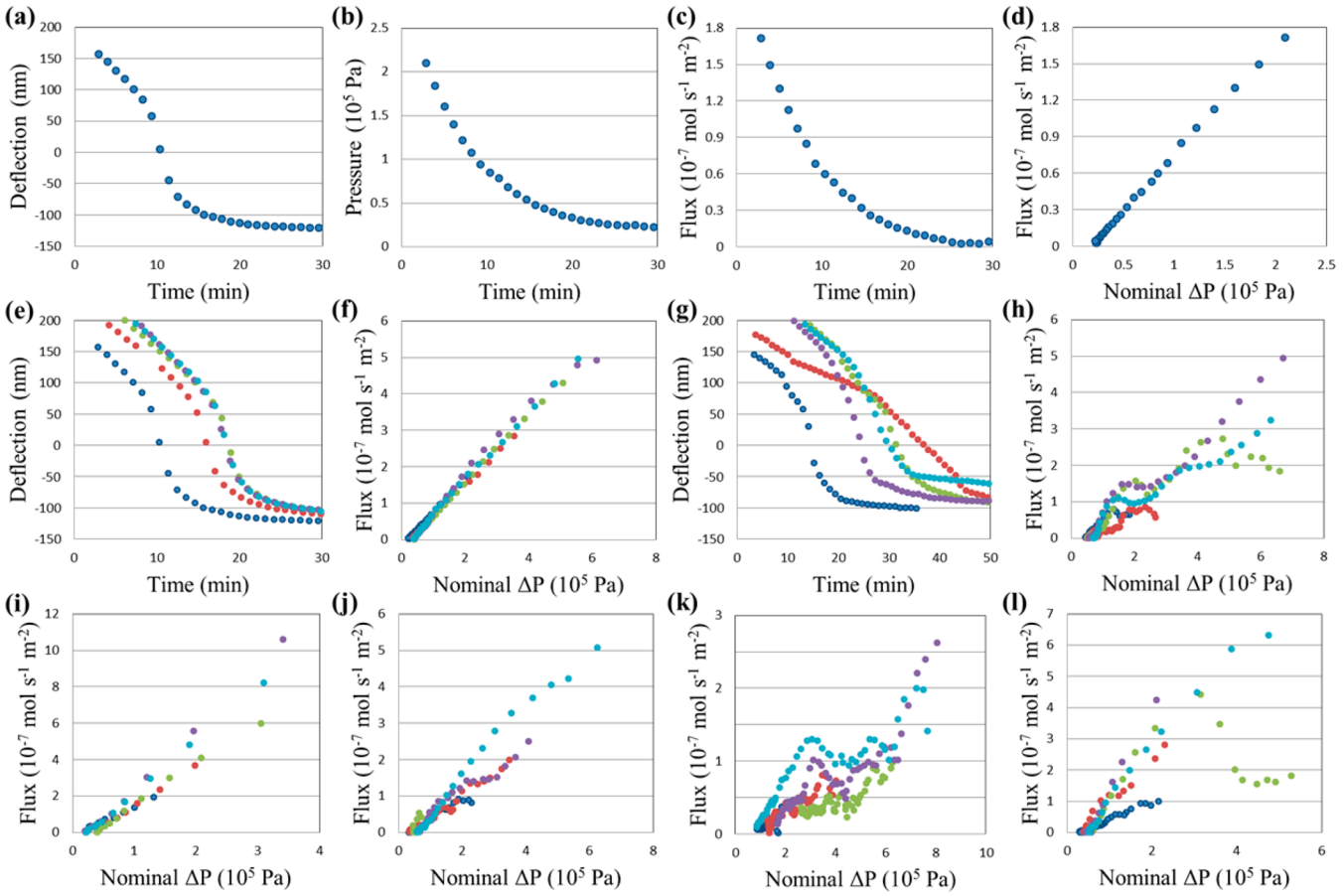

Figure 2. (a) Measured deflection versus time, (b) calculated microcavity pressure versus time, (c) calculated gas flux versus time, and (d) flux versus driving pressure difference for He transport with an initially observed pressure of 210 kPa (absolute). (e) Measured deflection versus time and (f) flux versus pressure difference for five sets of He experiments with initial pressures in the range 210−555 kPa; demonstrates expected linear behavior for flux versus pressure. (g) Measured deflection versus time and (h) flux versus pressure difference for five sets of H_2 experiments with initial pressures in the range 100−670 kPa; demonstrates some deviations from the general expected linear behavior for flux versus pressure. (a−h) Data collected from sample 1, a single layer graphene device. Flux versus pressure difference for (i) He, (j) H_2, (k) Ne, and (l) CO_2 were collected with sample 2, a bilayer graphene device.

In order to obtain a value for the gas flow (dn/dt) out of the chamber, the differential is applied to eq 3, with the dependence of pressure and volume on deflection emphasized.

$$\frac{dn(t)}{dt} = \frac{1}{RT}\frac{d\delta(t)}{dt}\frac{d(P(\delta)\,V(\delta))}{d\delta} \tag{5}$$

Equation 5 provides a method to use the slope of the measured deflection versus time to extract the instantaneous flow of gas out of the etched pore as a function of pressure. For this work, we used a rearrangement of this equation that enabled extracting values from the data using a linear least-squares fit.[30] With these relations, we follow the permeation behavior of the gas over the time just from the AFM measurements of deflection versus time.

Figure 2a−d demonstrates the use of the relations for a single experimental run with He gas. The experimental deflection data in Figure 2a is used to calculate the pressure and flux, molar flow normalized by membrane area, in (b) and (c) at each time point. Equation 5 can be utilized to investigate the transport mechanism by examining the dependence of the flux versus pressure, as done in Figure 2d, corresponding to the data in Figure 2a. This plot of flux versus pressure difference can help confirm the primary mechanism of gas permeation. The linearity of plot Figure 2d, for example, is consistent with nanopore transport (effusion) or Knudsen diffusion through the pore. Nanopore transport with molecular sieving is confirmed as the mechanism by showing that the ratio of permeance values exceeds Knudsen selectivities, which are determined by the inverse square root of molecular weight ratio for the series of gases.[30] The linearity rules out Poiseuille flow through a larger orifice which would demonstrate a quadratic dependence on pressure.

Furthermore, for the same membrane, the correlation between flux and pressure difference should be identical for all experiments. This is exactly what is seen in Figure 2f, a collection of five experiments for He. For the five experiments of H_2 in Figure 2h, however, the curves for each experiment do not overlap perfectly with another; and there are seemingly random divergences from perfect linearity, even if the general trend is still linear. These divergences appear stochastic, and are uncorrelated to pressure or mechanical position of the graphene. In considering the reason for these divergences, we first consider the corresponding measured deflection data used to calculate flux, shown in Figure 2e and g.

In Figure 2e, the deflection curves are all self-similar, which we define as having identical functional dependences translated along time axis according to the initial pressure only. In gas transport theory, the rate of isothermal transport is a function

DOI: 10.1021/acsnano.5b05870
ACS Nano XXXX, XXX, XXX−XXX

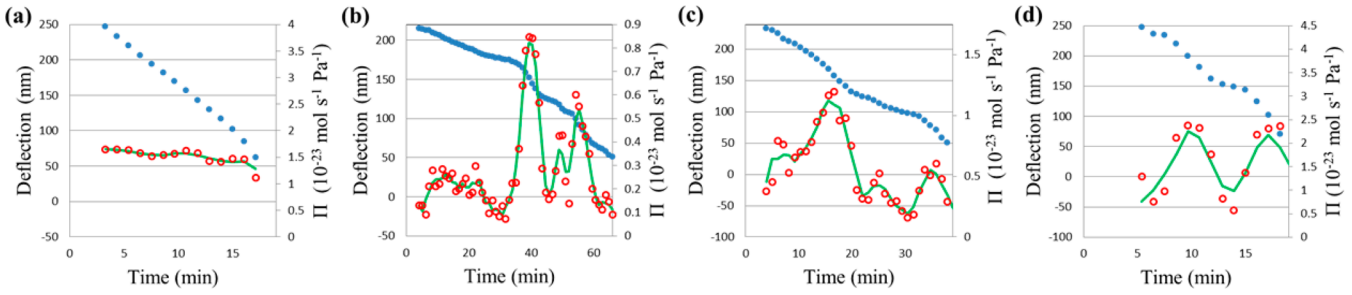

Figure 3. Deflection (blue closed circles) and permeance (red open circles) versus time over experiment for examples runs with (a) He, (b) Ne, (c) CO_2, and (d) H_2 with sample 1. The green line is a smoother fit of permeance, using additional points when fitting the slope. Demonstrates that kinks and changes in slope in the measured deflection that are indicative the corresponding changes in permeance.

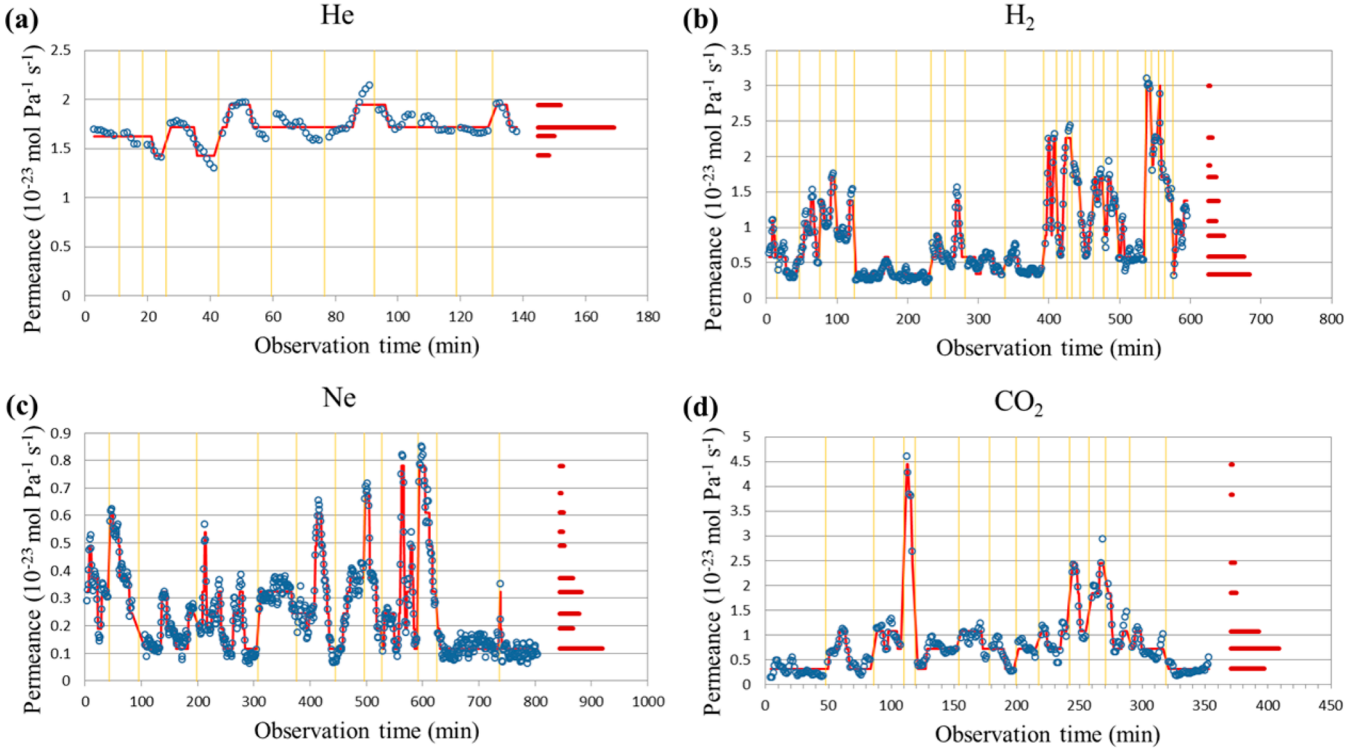

Figure 4. Permeance versus time for all experiments (blue open circles) concatenated for each of (a) He, (b) H_2, (c) Ne, and (d) CO_2 with sample 1. Red lines represent a hidden Markov model fit to discrete states. Bars in the right of each pane represent time spent in each fitted state. Orange vertical lines mark the transitions where data was merged between different experimental runs.

of the chemical potential difference across the pore, which simplifies to the partial pressure difference for low to moderate total pressure. Note that even for a strongly adsorbing gas, the transport rate is still a function of pressure only under these conditions (related through the adsorption isotherm). Figure 2g gives examples of deflection data for H_2 that is not self-similar, which we will explore in the following section.

A Mathematical Interpretation of Intersecting Deflection Curves. In understanding Figure 2e, it is useful to consider the following mathematical derivation, which shows that deviations from self-similarity in these curves mean that the transport rate is varying temporally, independently of pressure. We define a generic pressure dependence of a single component molar flow, $f(P)$, across the pore such that the differential equation describing the deflating microcavity system becomes

$$\frac{dn}{dt} = f(P) \tag{6}$$

Note that this function encompasses all versions of adsorption and diffusion models possible for the membrane system, and incorporates all possible rate limiting steps from our previous analytical work.[8] Rewriting eq 6 in terms of the deflection via the idea gas law yields eq 7.

$$\frac{dn}{dt} = \frac{1}{RT}\frac{d\delta}{dt}\frac{d(P(\delta)\,V(\delta))}{d\delta} = f(P(\delta)) \tag{7}$$

Note that this generic form remains separable such that upon integration:

$$\int_{\delta_0}^{\delta} \frac{1}{f(P(\delta))RT}\frac{d(P(\delta)V(\delta))}{d\delta}d\delta = \int_0^t dt \tag{8}$$

Defining the solution of the left integral as a generic function $G(\delta)$ we find that

$$G(\delta) - G(\delta_0) = t \tag{9}$$

Applying the inverse of the generic function,

DOI: 10.1021/acsnano.5b05870
ACS Nano XXXX, XXX, XXX−XXX

$$\delta = G^{-1}(t + G(\delta_0)) \tag{10}$$

The functional form of eq 10 describes curves of deflection versus time that are identical except for a shift in along the time axis given by the constant $G(\delta_0)$, which is a function of the initial pressure, and matches the definition for self-similarity. This is indeed the case for He, shown in Figure 2d, with a corresponding linearity between flux and pressure that reveals a constant, time invariant slope, as predicted by eq 10. It then follows that the departure from self-similarity in Figure 2g means that $f(P,t)$, or that the transport of gas has some time dependence (the only remaining dependent variable) outside of the expected pressure dependence. Hence, we take the intersecting deflection curves to imply:

$$\frac{dn}{dt} = \Pi(t)\Delta P \tag{11}$$

We consider the flow of gas in terms of what we define as the membrane permeance, with the molar rate normalized by the pressure difference. A typical membrane will have a constant permeance, corresponding to a linear molar flow with pressure. To account for the time dependent behavior of the transport, we modify our expectation of the molar flow rate, dn/dt, so that it includes a time dependent permeance, $\Pi(t)$, for cases where self-similarity does not appear to be observed.

For the case of He, with its self-similar deflection curves, the permeance, $\Pi(t)$, remains essentially constant with time. However, the permeances for other data sets, H_2, Ne, and CO_2, show obvious variation in time. Figure 3 shows a few examples of the variation in permeance with time, plotted alongside the experimentally measured deflection curves. Figure 3a, an example data set for an experimental run with He, shows that the permeance remains mostly constant. In the other panels, there are sharp changes that occur at various times. These are discrete changes in the values permeance and correspond to kinks and changes in slope of the deflection curves. They typically appear smoothed even though the changes are discrete because the fitting method used to extract the permeance values must fit the slope across multiple points; Figure 3 shows two levels of smoothing, red dots with low smoothing from using only three points to extract permeance, and a green line with more smoothing using five points in the extraction.

Hidden Markov Analysis of Time Dependent Permeance. Each individual experimental run is isolated by the preparatory step of repressurizing the microcavity. However, all experiments are performed on the same membrane, and therefore, we assume that the observed transport properties are consistent across all experimental runs for a given gas. To visualize trends, we have concatenated the data from each run with that gas species into a single time axis referred to as "observation time" in Figure 4. We included only data points corresponding to measured deflections above 50 nm, as points at low deflections were more sensitive to experimental error; and permeance was extracted by using five data points, equivalent to the green line of Figure 3. To help analyze and fit the data to discrete states, we employed hidden Markov modeling via the program HaMMy.[32] This fits the permeance data to up to ten discrete states with instantaneous transitions between them. Some of these transitions fall at the time points corresponding to breaks between experimental runs, but these transitions were excluded from later quantitative analysis of transition frequency.

In Figure 4, the data sets corresponding to H_2, Ne, and CO_2 all show large changes in permeance up to around a factor of 10, and multiple states are observed, with HaMMy fitting between 7 and 10 states. Many examples of state switching in pores occur as two states, and more observed states are the result of multiple two-state pores. To investigate whether multiple pores could be responsible for the many states observed in Figure 4, we looked at the relations given by the Markov network for a fixed number of pores and applied analysis based on them to the data. With multiple two-state pores, two pores yields four possible observed states, three pores yields eight possible observed states, four yields 16 possible observed states, and so on. A three pore system has a comparable number of states to those from HaMMy fitting, therefore our analysis focuses on matching a three pore system.

Three Pore Model. For evaluating goodness of fit for the data to the three pore model, the constraints imposed on the observed state permeance level and state transitions are what differentiate the alternate hypothesis of fewer than three pores having many states. The first step in evaluating those properties is to describe the system by eight states, which are determined by four underlying parameters. The eight states correspond to the possible combinations of the two-state pores, which we describe as having "high" and "low" permeance states. How well the data can be fit by these four parameters can be one test of the three pore hypothesis. The relations that describe the eight observed permeance states are described by the matrix problem in eq 12; x is the combined permeance of the low states for all three pores; y_a, y_b, and y_c are the difference between the high and low states for the first, second, and third pores, respectively; and Π_j is the permeance value for the jth observable state.

$$\begin{pmatrix} y_a \\ y_b \\ y_c \end{pmatrix} \begin{pmatrix} 0 & 0 & 0 \\ 1 & 0 & 0 \\ 0 & 1 & 0 \\ 0 & 0 & 1 \\ 1 & 1 & 0 \\ 1 & 0 & 1 \\ 0 & 1 & 1 \\ 1 & 1 & 1 \end{pmatrix} + x = \begin{pmatrix} \Pi_1 \\ \Pi_2 \\ \Pi_3 \\ \Pi_4 \\ \Pi_5 \\ \Pi_6 \\ \Pi_7 \\ \Pi_8 \end{pmatrix} \tag{12}$$

With the convention that $y_a < y_b < y_c$, the permeance values Π_j in eq 12 are always ordered in increasing permeance with the exception of Π_4 and Π_5, the order of which should be swapped if $(y_a + y_b) < y_c$. Table 1 summarizes the set of relations described by eq 12 under the column for observed permeance.

After defining the permeance levels of the states, we move on to look at the dwell times and transitions. Ideally, the statistics of the transitions from state to state can show unique characteristics of a three pore system, however the transitions are more difficult to use as a distinguisher because of the effects of smoothing that occurs from the calculation of permeance from deflection and the fact that the full data set is a concatenation of many shorter, isolated segments of AFM measurements. However, the dwell time, in particular the total time spent in each state, is relatively unaffected by those issues and is useful as a distinguishing measure.

DOI: 10.1021/acsnano.5b05870
ACS Nano XXXX, XXX, XXX−XXX

Table 1. Summary of Nomenclature Defined in Eqs 12–22 with Illustrations Showing the Corresponding Pore Configurations

Individual pore			
State	Pore	Individual permeance	Fraction of total time spent in state
"Low"		x_a	$(1- p_a)$
"High"		$x_a + y_a$	p_a

Observed states (three pores)					
State	Pores			Observed permeance	Fraction of total time spent in state
	a	b	c		
1				$\Pi_1 = x_a+x_b+x_c=x$	$P_1=(1-p_a)(1-p_b)(1-p_c)$
2				$\Pi_2 = x + y_a$	$P_2 = p_a (1-p_b)$
3				$\Pi_3 = x + y_b$	$P_3 = (1-p_a)\, p_b\, (1-p_c)$
4				$\Pi_4 = x + y_c$	$P_4 = (1-p_a)\, (1-p_b)\, p_c$
5				$\Pi_5 = x + y_a + y_b$	$P_5 = p_a\, p_b\, (1-p_c)$
6				$\Pi_6 = x + y_a + y_c$	$P_6 = p_a\, (1-p_b)\, p_c$
7				$\Pi_7 = x + y_b + y_c$	$P_7 = (1-p_a)\, p_b\, p_c$
8				$\Pi_8 = x + y_a + y_b + y_c$	$P_8 = p_a\, p_b\, p_c$

In our analysis, we define the lower case p_i to be the fraction of time a single pore, in this case pore a, b, or c, spends in its high permeance state, given by eq 13, where t_i is the time spent in the high permeance state of the ith pore and t_{total} is the total time. It can also be considered the probability of finding the pore in its high permeance state.

$$p_i = \frac{t_i}{t_{total}} \tag{13}$$

p_i as defined by eq 13 is an underlying property of an individual pore, related to the thermodynamic equilibrium and free energy difference between the two states; it is not directly related to a single observable state, as the observed states come from a combination of pores; it can be calculated as a sum of observed state times, or from other relations as shown below. We use the capitalized P_j of eq 14 to indicate the fraction of time spent in each observable state, where t_j is time spent in the jth observed state from experimental results.

$$P_j = \frac{t_j}{t_{total}} \tag{14}$$

The fraction of time in each of the eight observable states, the eight P_j, should be related to the probabilities the individual pores are in their high permeance states. The relations are described by eqs 15–22 and are also summarized in Table 1 under the column for fraction of time spent in state.

$$P_1 = P_{000} = (1 - p_a)(1 - p_b)(1 - p_c) \tag{15}$$

$$P_2 = P_{100} = p_a(1 - p_b)(1 - p_c) \tag{16}$$

$$P_3 = P_{010} = (1 - p_a)p_b(1 - p_c) \tag{17}$$

$$P_4 = P_{001} = (1 - p_a)(1 - p_b)p_c \tag{18}$$

$$P_5 = P_{110} = p_a p_b(1 - p_c) \tag{19}$$

$$P_6 = P_{101} = p_a(1 - p_b)p_c \tag{20}$$

$$P_7 = P_{011} = (1 - p_a)p_b p_c \tag{21}$$

$$P_8 = P_{011} = p_a p_b p_c \tag{22}$$

From eqs 15–22, the probability that each of the pores is in the high state (p_a, p_b, and p_c) can be found by solving the system of nonlinear equations for these three variables, as done below. These parameters are related to four of the P_j values analytically via:

$$p_a = \frac{P_8}{P_7 + P_8} \tag{23}$$

$$p_b = \frac{P_8}{P_6 + P_8} \tag{24}$$

$$p_c = \frac{(P_6 + P_8)(P_7 + P_8)}{P_8} \tag{25}$$

A shorthand check of whether the calculated P_j values describe a three pore system is found by four analytical eqs 26–29 that relate their values in the case of the three pore system:

$$\left(\frac{P_8}{P_7 + P_8}\right) = \left(\frac{P_2}{P_1 + P_2}\right) \tag{26}$$

$$\left(\frac{P_8}{P_6 + P_8}\right) = \left(\frac{P_3}{P_1 + P_3}\right) \tag{27}$$

$$\left(\frac{(P_6 + P_8)(P_7 + P_8)}{P_8}\right) = \left(1 - P_1 - P_2 - \frac{(P_1 + P_2)P_3}{P_8}\right) \tag{28}$$

$$\left(\frac{P_3}{P_1 + P_3}\right) = \left(\frac{(P_3 + P_7)(P_7 + P_8)}{P_7}\right) \tag{29}$$

Comparison to Simulated Data Sets. Going further in order to establish confidence in assignment to a three pore system, we used a Monte Carlo approach to generate simulated data in the form of the experimentally obtained permeance versus time. First we simulated data corresponding to three independent pores, as described by the equations of the previous section, summarized in Table 1; we refer to these as "positive simulations." At each fixed time step, each of the three pores had a given probability of changing its state from high to low, or low to high. The probabilities of both those transitions are distinct, meaning six probabilities are used to control the transitions to and average time spent in each state. In addition to six probabilities, a variable for each of the three pores, y_a, y_b, and y_c, describes the difference between that pore's high and low permeance states, and the overall lowest observed permeance state, x, is described by a single variable. With values for these parameters, we simulated permeance versus time points for the same number of time points as the experimental data set. Each point of data was smoothed by averaging the four closest points in time to emulate the smoothing that results from the calculation of permeance from experimentally measured deflection of graphene over the

DOI: 10.1021/acsnano.5b05870
ACS Nano XXXX, XXX, XXX−XXX

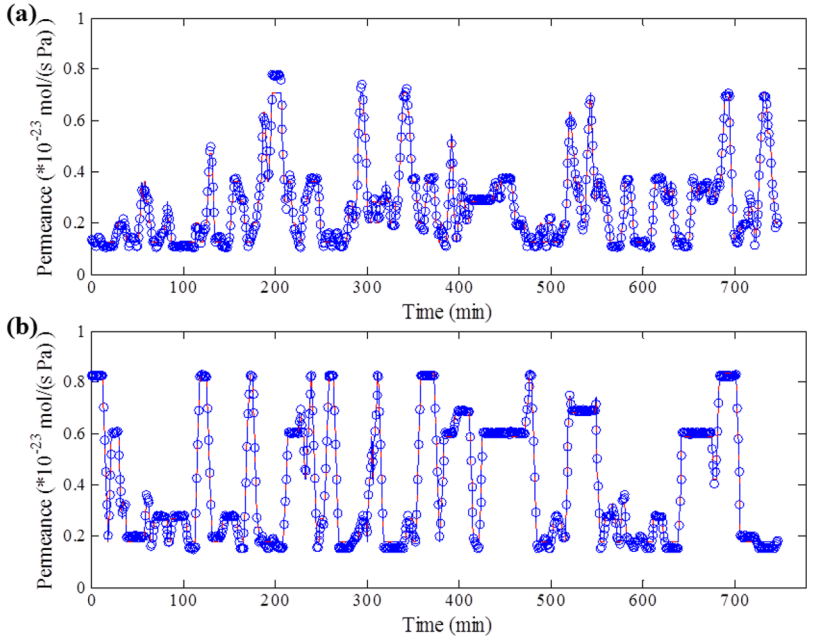

Figure 5. (a) Example simulated data set generated using three pore model, positive simulation. (b) Example simulated data set generated with eight states unconstrained by three pore model relations, negative simulation.

microcavity. A small amount of random Gaussian noise was also added to the simulated permeance data set. The total number of simulated data points was set to 700 to match the size of the experimental Ne data set, as the size of the data set is an important factor in the level of confidence that can be achieved. The top pane of Figure 5 shows an example simulated data set generated with the three pore model.

For the case of three independent pores, the observed permeance levels and state probabilities are constrained by the relations in eqs 12 and 15−22 and determined by the hidden parameters for the three pores; in a system with eight uncorrelated states, the observed states would not be bound by those relations. In an equivalent manner as the previous described positive simulations case, alternate simulations were carried out such that there were eight states with independent parameters, unconstrained by the relations of a three pore system; we refer to such simulations as "negative simulations." The resulting simulated data sets were qualitatively similar the experimentally obtained permeance versus time. Figure 5b gives an example data set from a negative simulation. To test the hypothesis and evaluate the confidence in assigning the experimental system as three pore, we performed 450 negative simulations with eight states not constrained to a three pore system and 150 simulations of a model three pore system. These sets of simulations were generated with parameters that would result in data qualitatively similar to the experimental data in terms of the frequency of transitions; full details of parameters of simulations can be found in the Supporting Information.

For analyzing either the experimental data sets or simulated data, the data set was fit with a least-squares approach to the eight states using the definition of sum squared error, SSE_{Π}, defined by eq 30, where N is the total number of permeance data points, $\Pi(t_k)$ is the permeance value at a given time point t_k, and the set of $\Pi_j(x, y_a, y_b, y_c)$ are the model permeance states defined by eq 12.

$$SSE_{\Pi} = \sum_{k=1}^{N} \min_{j=1}^{8} \{(\Pi(t_k) - \Pi_j(x, y_a, y_b, y_c))^2\} \tag{30}$$

After fitting permeance data points to the model states as described above, we then assigned each point to a given state and calculated fraction of time spent in each observed state, P_j as described in eq 14. To provide a measure of the goodness of fit to three pores, we then applied a second least-squares fit on the eight values of time spent in each state, P_j. The sum of squared error for this fit, SSE_P, is described in eq 31,

$$SSE_P = \sum_{j=1}^{8} (P_{j,\mathrm{obs}} - P_j(p_a, p_b, p_c))^2 \tag{31}$$

where $P_{j,\mathrm{obs}}$ is the value calculated directly from the data set and $P_j(p_a,p_b,p_c)$ is the value calculated appropriate expression in eqs 15−22, with p_a, p_b, and p_c varied as parameters for the least-squares optimization.

The sum of squared error for this fit, SSE_P from eq 31, provides a measure for the goodness of fit to three pores; there are eight values of fraction time spent for the eight observed states fitted with least-squares using three parameters. We preferred this distinguisher when comparing the analysis between simulation and experimental results, as it is less sensitive to the magnitude of noise in the permeance values. The histogram in Figure 6 compares the distribution of SSE_P values between the positively and negatively generated data sets, as well as marks the experimental value for the Ne data sets with a vertical line. There is significant overlap between the two sets, meaning distinguishing between the two is often difficult for data sets of this size; however, the evaluation of the SSE_P for the experimental data shows that it can be distinguished in this case. The experimental data set for Ne lies at the 15th percentile for positive simulations of the same number of data points as collected for Ne, placing them within the typical range of simulations. For the negative simulations, not generated with a three pore model, the experimental results

DOI: 10.1021/acsnano.5b05870
ACS Nano XXXX, XXX, XXX−XXX

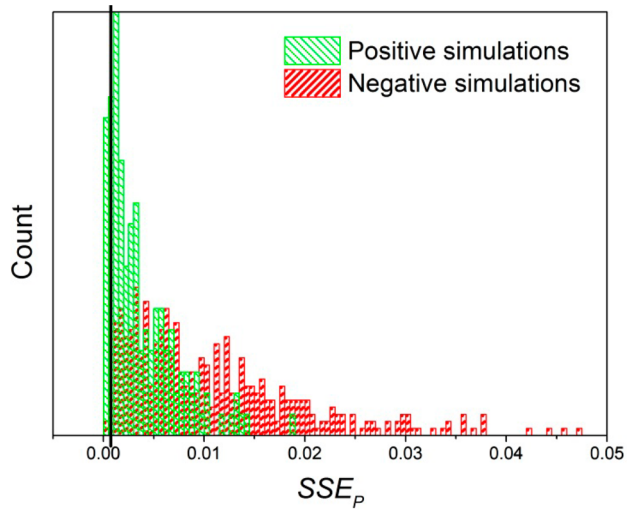

Figure 6. Histogram of the sum squared errors (SSE_P) when fitting fraction of time spent to three pore model. Positive simulations (green) are generated by a mock three pore system; negative simulations (red) are generated with randomized parameters for eight states unconstrained by three pore relations. The vertical black line represents locations of experimental results for Ne with sample 1.

were at the first percentile, being a better fit than nearly all of the simulated data sets. This allows us to place a high degree of confidence in our statement that the experimental sample is consistent with a three pore system. Additional simulations summarized in the Figure S1 of the Supporting Information show that the overlap and spread of the positive simulations results from the finite size of the data set, and the smoothing/noise inherent to the analysis of the experimental data or intentionally added in simulations.

The coefficient of determination, R^2, from both the least-squares fitting of the states permeance levels, SSE_Π, and the fitting of fraction of time spent in each state, SSE_P, and the resulting fitted values for the individual pores are summarized in Table 2. As shown in Figure 4a, He did not exhibit significant state switching behavior and its fit is included only for comparison. The assignment of fitted values to pores a, b, or c was done according to increasing y values, the difference between the permeance of high and low states, assuming the trend is consistent between the gases. The exact values of x and the three y_i should not be the same for different gases, or even necessarily scale proportionally, as the interaction between the pore and the gas molecule is not simple. However, the three values of p_i, the likelihoods of the individual pores being in a high or low state, are likely to be properties of the pores themselves; and the fact that the three p_i values are similar between the three different gases is consistent with this interpretation. A more specific interpretation for the meaning of the p_i values is given in the below section.

Mechanism for Switching. The transport through the pore is limited by the energy barrier the molecule experiences when passing through the pore, as the separation factors between gases exceed the molecular weight based Knudsen selectivities from an effusion mechanism.[30] This barrier energy is different for each molecule-pore combination, and the differences in the barrier energy between molecules are the source of the observed high selectivities. We explain the observed permeance switching as the result of a small rearrangement in the pore, in essence a small chemical change, that alters the energy barrier that the gas molecules experience passing through the pore. Because of the strong dependence on the energy barrier, relatively small changes in the pore can effect a large change in permeance. The large stochastic changes in permeance observed are a direct effect of these molecular scale rearrangements at the pore.

With this view of the switching, we can define clearer meaning to the p_i values used in the model of the previous section. The p_i values define the fraction of time the pore spends in each state, and they effectively represent the thermodynamic chemical equilibrium between the two pore configurations, ultimately a function of the relative free energies of the two configurations. The differences between p_a, p_b, and p_c, the values for the three pores, in Table 2, stem from differences in the configurations and energies of the three individual pores. The fact that variance for a specific p_i value across the studied gases with observed fluctuations is much smaller compared to the variance across pores is consistent with this interpretation of stochastic changes in pore configuration.

Additionally, in Figure 4a, the large jumps in permeance are not observed for He. We explain this as a result of the fact that He is the smallest gas tested, significantly smaller than the pore compared to the other gases, and it thus experiences a very small or no barrier to transport through the pore. Because the molecule is significantly smaller than the pore, the slight rearrangement in the pore edges does not significantly affect the barrier energy and therefore does not result in a large permeance change. For the other gases, whose sizes are more commensurate with the pore, the small changes in pore size and chemistry are more impactful. Figure 7 uses Lennard–Jones potentials[33,34] to calculate the energy barriers for two configurations of a toy pore and demonstrates that He is insensitive to the small change between the two configurations, whereas the predicted permeance change is comparable to the experimentally observed permeance fluctuations for the other gases tested.

Table 2. Summary of Three Pore Model Fitting for Experimental Results for the Experimentally Measured Gases with Sample 1[a]

		R^2					10^{-23} mol/(s Pa)			
gas	N	SSE_Π	SSE_P	p_a	p_b	p_c	x	y_a	y_b	y_c
Ne	699	0.97	0.99	0.38	0.37	0.11	0.11	0.08	0.18	0.40
H_2	484	0.97	0.99	0.46	0.28	0.11	0.32	0.32	0.71	1.47
CO_2	288	0.95	0.96	0.50	0.21	0.04	0.28	0.49	0.89	2.23
He	109	0.97	0.50	0.36	0.32	0.72	1.36	0.15	0.25	0.32

[a] N is the number of data points; R^2 is the coefficient of determination calculated with the appropriate sum of squared error; SSEΠ is defined by eq 30; SSE_P is defined by eq 31; the three p_i are defined by eq 13; x and the three y_i are used and defined by eq 12.

DOI: 10.1021/acsnano.5b05870
ACS Nano XXXX, XXX, XXX−XXX

(a) (b)

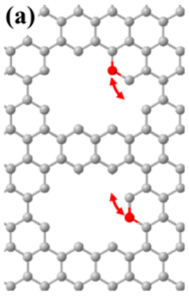

Gas	Calculated energy barrier /(R*298 K) Bottom pore	Top pore	Expected ratio of permeances (top/bottom)
He	0	0	1.0
Ne	0	0.7	0.5
H_2	0	1.1	0.3
O_2	7.3	23.8	7×10^{-8}
Ar	8.6	25.7	4×10^{-8}
N_2	14.5	36.8	2×10^{-10}

Figure 7. (a) Example of a small scale rearrangement for a simplified model pore formed from eight carbon atom vacancies. (b) Estimations for energy barrier for gas transport and the associated ratios of expected permeances for He, Ne, H_2, O_2, Ar, and N_2 gases.

The frequency at which the switching between permeance states occurs can be used to gain a rough estimate of the activation energy for the pore rearrangement. Counting the number of transitions from the Hidden Markov fits for H_2, Ne, and CO_2, while excluding any transitions that occur where separate experimental runs are merged together, transitions in permeance states occurred every 15 min on average. Considering that three pores are responsible for the transitions, we use an average frequency for the forward transition of 45 min. By assuming an Arrhenius dependence with an attempt frequency of 10^{13} 1/s, corresponding to the order of magnitude for molecular vibrations,[35] we calculate an activation energy for switching to be 1.0 eV. This value is commensurate with activation energies for bond rearrangements, such as cis−trans isomerization,[36] which is consistent with the proposed mechanism of small scale rearrangements giving rise to the observed switching in permeance.

CONCLUSIONS

In conclusion, the technique of measuring gas permeance through AFM measured changes in the bulge deflection over time can be used to extract the permeance and the gas transport characteristics. Further, we demonstrated the permeance can be tracked over time and revealed stochastic and discrete changes among difference states with large changes in permeance. Through analysis based on a three pore Markov network, we showed that the multiple observed states arose from a combination of three independent pores alternating between two states; comparing to simulated data sets to show the quality of the experimental data's fit was within expectations, 15th percentile, for a three pore Markov network and outside the range of that for a nonthree pore controls, first percentile. We attributed the source of the fluctuating states for the individual pores to small scale rearrangement in the pore structure, and could estimate the activation energy for switching as 1.0 eV, comparable to the energy required for a bond rearrangement. This work highlights the value in the study and consideration of pore stability in theoretical work on graphene membranes, and emphasizes that pore stability and averaging across configurations may play an important role in determining the performance of large scale membranes. This work details the analysis of the first time stochastic state switching has been observed in a gas phase system, and the extraordinary sensitivity of the gas permeance and the localization of the transport at a single point gives this platform potential to be applied to issues of sensing and nanoscale material management, such as "nanoprinting" or nanocatalysis.

EXPERIMENTAL METHODS

The experimental data for this analysis was collected on the same device as presented in the recent paper by the Bunch group,[30] and is an extension of previous methods.[24,29] In summary, microcavities approximately 800 nm deep and 5 μm in diameter are formed in grid an oxidized silicon wafer by reactive ion etching, and mechanically exfoliated graphene is deposited on top. Regions of monolayer or bilayer graphene are identified optically and by Raman spectroscopy. The graphene effectively isolates the microcavities from atmosphere, but with diffusion though the silicon dioxide surface, the cavity will equilibrate with their surroundings over the course of days. By placing the sample in a vacuum or pressurized chamber, specific gases can be removed or added to the microcavity at the given pressure. For a pressurized sample, after removing from the pressurized chamber, atomic force microscopy (AFM) measurements show an upward deflection in the graphene surface above a chosen microcavity from the difference between the pressure inside the microcavity and atmospheric. Likewise, the graphene surface deflects downward after being removed from a vacuum chamber. To form a pore, the sample is exposed ultraviolet induced oxidative etching in 30 or 45 s intervals. Before exposure, the sample is pressurized with H_2 gas, giving an upward deflection. Between etching exposures, the sample is checked with AFM to check if the deflection had changed significantly, indicating a pore formation event somewhere in the graphene covering the microcavity. Once a pore forms, the deflection starts to change rapidly and etching is typically ceased. After the etching and pore formation, the microcavity pressurizes and deflates much more rapidly, over the course of minutes to hours depending on the gas species used. The sample can then be repeatedly pressurized and its deflation over time measured with AFM in order to study the transport characteristics through the pore(s) formed. The initial pressurization corresponding to the deflection at the start of AFM measurements ranged from 100 to 670 kPa, with the upper bound limited to avoid delamination of the graphene from the surface, as seen in previous work.[29] The delay between removing the sample from the pressure chamber and AFM measurement was typically around 5 min.

ASSOCIATED CONTENT

Supporting Information

The Supporting Information is available free of charge on the ACS Publications website at DOI: 10.1021/acsnano.5b05870.

Simulation details and parameters; additional simulation results (PDF)

AUTHOR INFORMATION

Corresponding Author

*E-mail: strano@mit.edu.

Notes

The authors declare no competing financial interest.

ACKNOWLEDGMENTS

This research was supported (in part) by the U.S. Army Research Office under contract W911NF-13-D-0001.

REFERENCES

(1) Bunch, J. S.; Verbridge, S. S.; Alden, J. S.; van der Zande, A. M.; Parpia, J. M.; Craighead, H. G.; McEuen, P. L. Impermeable Atomic Membranes from Graphene Sheets. *Nano Lett.* **2008**, *8*, 2458−62.

(2) Hu, S.; Lozada-Hidalgo, M.; Wang, F. C.; Mishchenko, A.; Schedin, F.; Nair, R. R.; Hill, E. W.; Boukhvalov, D. W.; Katsnelson, M. I.; Dryfe, R. A. W.; Grigorieva, I. V.; Wu, H. A.; Geim, A. K. Proton Transport through One-Atom-Thick Crystals. *Nature* **2014**, *516*, 227−230.

DOI: 10.1021/acsnano.5b05870
ACS Nano XXXX, XXX, XXX−XXX

(3) Schrier, J. Carbon Dioxide Separation with a Two-Dimensional Polymer Membrane. *ACS Appl. Mater. Interfaces* **2012**, *4*, 3745−3752.
(4) Ambrosetti, A.; Silvestrelli, P. L. Gas Separation in Nanoporous Graphene from First Principle Calculations. *J. Phys. Chem. C* **2014**, *118*, 19172−19179.
(5) Schrier, J. Helium Separation Using Porous Graphene Membranes. *J. Phys. Chem. Lett.* **2010**, *1*, 2284−2287.
(6) Shan, M.; Xue, Q.; Jing, N.; Ling, C.; Zhang, T.; Yan, Z.-F.; Zheng, J. Influence of Chemical Functionalization on the CO(2)/N(2) Separation Performance of Porous Graphene Membranes. *Nanoscale* **2012**, *4*, 5477−82.
(7) Liu, H.; Dai, S.; Jiang, D.-e. Insights into CO2/N2 Separation through Nanoporous Graphene from Molecular Dynamics. *Nanoscale* **2013**, *5*, 9984−9987.
(8) Drahushuk, L. W.; Strano, M. S. Mechanisms of Gas Permeation through Single Layer Graphene Membranes. *Langmuir* **2012**, *28*, 16671−16678.
(9) Sun, C.; Boutilier, M. S. H.; Au, H.; Poesio, P.; Bai, B.; Karnik, R.; Hadjiconstantinou, N. G. Mechanisms of Molecular Permeation through Nanoporous Graphene Membranes. *Langmuir* **2014**, *30*, 675−682.
(10) Liu, H.; Dai, S.; Jiang, D.-e. Permeance of H2 through Porous Graphene from Molecular Dynamics. *Solid State Commun.* **2013**, *175*−*176*, 101−105.
(11) Blankenburg, S.; Bieri, M.; Fasel, R.; Müllen, K.; Pignedoli, C. a.; Passerone, D. Porous Graphene as an Atmospheric Nanofilter. *Small* **2010**, *6*, 2266−71.
(12) Jiang, D.-e.; Cooper, V. R.; Dai, S. Porous Graphene as the Ultimate Membrane for Gas Separation. *Nano Lett.* **2009**, *9*, 4019−24.
(13) Liu, H.; Chen, Z.; Dai, S.; Jiang, D.-e. Selectivity Trend of Gas Separation through Nanoporous Graphene. *J. Solid State Chem.* **2015**, *224*, 2−6.
(14) Du, H.; Li, J.; Zhang, J.; Su, G.; Li, X.; Zhao, Y. Separation of Hydrogen and Nitrogen Gases with Porous Graphene Membrane. *J. Phys. Chem. C* **2011**, *115*, 23261−23266.
(15) Lei, G.; Liu, C.; Xie, H.; Song, F. Separation of the Hydrogen Sulfide and Methane Mixture by the Porous Graphene Membrane: Effect of the Charges. *Chem. Phys. Lett.* **2014**, *599*, 127−132.
(16) Tao, Y.; Xue, Q.; Liu, Z.; Shan, M.; Ling, C.; Wu, T.; Li, X. Tunable Hydrogen Separation in Porous Graphene Membrane: First-Principle and Molecular Dynamic Simulation. *ACS Appl. Mater. Interfaces* **2014**, *6*, 8048−8058.
(17) Li, Y.; Zhou, Z.; Shen, P.; Chen, Z. Two-Dimensional Polyphenylene: Experimentally Available Porous Graphene as a Hydrogen Purification Membrane. *Chem. Commun. (Cambridge, U. K.)* **2010**, *46*, 3672−4.
(18) Cohen-Tanugi, D.; Grossman, J. C. Water Desalination across Nanoporous Graphene. *Nano Lett.* **2012**, *12*, 3602−8.
(19) Konatham, D.; Yu, J.; Ho, T. A.; Striolo, A. Simulation Insights for Graphene-Based Water Desalination Membranes. *Langmuir* **2013**, *29*, 11884−11897.
(20) Cohen-Tanugi, D.; Grossman, J. C. Water Permeability of Nanoporous Graphene at Realistic Pressures for Reverse Osmosis Desalination. *J. Chem. Phys.* **2014**, *141*, 074704.
(21) Fileti, E. E.; Dalpian, G. M.; Rivelino, R. Liquid Separation by a Graphene Membrane. *J. Appl. Phys.* **2010**, *108*, 113527.
(22) Hu, G.; Mao, M.; Ghosal, S. Ion Transport through a Graphene Nanopore. *Nanotechnology* **2012**, *23*, 395501.
(23) Sint, K.; Wang, B.; Král, P. Selective Ion Passage through Functionalized Graphene Nanopores. *J. Am. Chem. Soc.* **2008**, *130*, 16448−16449.
(24) Koenig, S. P.; Wang, L.; Pellegrino, J.; Bunch, J. S. Selective Molecular Sieving through Porous Graphene. *Nat. Nanotechnol.* **2012**, *7*, 728−732.
(25) O'Hern, S. C.; Stewart, C. A.; Boutilier, M. S. H.; Idrobo, J.-C.; Bhaviripudi, S.; Das, S. K.; Kong, J.; Laoui, T.; Atieh, M.; Karnik, R. Selective Molecular Transport through Intrinsic Defects in a Single Layer of CVD Graphene. *ACS Nano* **2012**, *6*, 10130−10138.
(26) Boutilier, M. S. H.; Sun, C.; O'Hern, S. C.; Au, H.; Hadjiconstantinou, N. G.; Karnik, R. Implications of Permeation through Intrinsic Defects in Graphene on the Design of Defect-Tolerant Membranes for Gas Separation. *ACS Nano* **2014**, *8*, 841−849.
(27) Walker, M. I.; Weatherup, R. S.; Bell, N. A. W.; Hofmann, S.; Keyser, U. F. Free-standing Graphene Membranes on Glass Nanopores for Ionic Current Measurements. *Appl. Phys. Lett.* **2015**, *106*, 023119.
(28) Celebi, K.; Buchheim, J.; Wyss, R. M.; Droudian, A.; Gasser, P.; Shorubalko, I.; Kye, J.-I.; Lee, C.; Park, H. G. Ultimate Permeation Across Atomically Thin Porous Graphene. *Science* **2014**, *344*, 289−292.
(29) Koenig, S. P.; Boddeti, N. G.; Dunn, M. L.; Bunch, J. S. Ultrastrong Adhesion of Graphene Membranes. *Nat. Nanotechnol.* **2011**, *6*, 543−546.
(30) Wang, L.; Drahushuk, L. W.; Cantley, L.; Koenig, S. P.; Liu, X.; Pellegrino, J.; Strano, M. S.; Bunch, J. S. Molecular Valves for Controlling Gas Phase Transport Made from Discrete ångström-sized Pores in Graphene. *Nat. Nanotechnol.* **2015**, *10*, 785−790.
(31) Bunch, J. S. *Mechanical and Electrical Properties of Graphene Sheets*, Ph.D. Thesis, Cornell University, Ithaca, NY, 2008.
(32) McKinney, S. A.; Joo, C.; Ha, T. Analysis of Single-Molecule FRET Trajectories Using Hidden Markov Modeling. *Biophys. J.* **2006**, *91*, 1941−1951.
(33) Reid, R. C.; Prausnitz, J. M.; Poling, B. E. *The Properties of Gases and Liquids*; McGraw-Hill: New York, 1987.
(34) Steele, W. A. *The Interaction of Gases with Solid Surfaces*; Pergamon Press: Oxford, U.K., 1974.
(35) Kolasinki, K. W. *Surface Science: Foundations of Catalysis and Nanoscience*; Wiley: Chichister, England; Hoboken, NJ, 2008.
(36) Cembran, A.; Bernardi, F.; Garavelli, M.; Gagliardi, L.; Orlandi, G. On the Mechanism of the cis−trans Isomerization in the Lowest Electronic States of Azobenzene: S0, S1, and T1. *J. Am. Chem. Soc.* **2004**, *126*, 3234−3243.

DOI: 10.1021/acsnano.5b05870
ACS Nano XXXX, XXX, XXX−XXX